

**Synthetic gauge field and chiral physics on two-leg superconducting circuits**Xin Guan<sup>1,\*</sup>, Yanlin Feng<sup>2</sup>, Zheng-Yuan Xue<sup>3,4,†</sup>, Gang Chen<sup>1,5,6,‡</sup> and Suotang Jia<sup>1,5</sup><sup>1</sup>*State Key Laboratory of Quantum Optics and Quantum Optics Devices, Institute of Laser Spectroscopy, Shanxi University, Taiyuan 030006, China*<sup>2</sup>*Shandong Provincial Engineering and Technical Center of Light Manipulations and Shandong Provincial Key Laboratory of Optics and Photonic Devices, School of Physics and Electronics, Shandong Normal University, Jinan 250014, China*<sup>3</sup>*Guangdong Provincial Key Laboratory of Quantum Engineering and Quantum Materials, GPETR Center for Quantum Precision Measurement, and School of Physics and Telecommunication Engineering, South China Normal University, Guangzhou 510006, China*<sup>4</sup>*Frontier Research Institute for Physics, South China Normal University, Guangzhou 510006, China*<sup>5</sup>*Collaborative Innovation Center of Extreme Optics, Shanxi University, Taiyuan, Shanxi 030006, China*<sup>6</sup>*Collaborative Innovation Center of Light Manipulations and Applications, Shandong Normal University, Jinan 250358, China*

(Received 22 March 2020; revised 22 August 2020; accepted 26 August 2020; published 8 September 2020)

The gauge field is essential for exploring novel phenomena in modern physics. However, it has not been realized in the recent breakthrough experiment on two-leg superconducting circuits with transmon qubits [Y. Ye *et al.*, *Phys. Rev. Lett.* **123**, 050502 (2019)]. Here we present an experimentally feasible method to achieve the synthetic gauge field by introducing ac microwave driving in each qubit. In particular, the effective magnetic flux per plaquette achieved can be tuned independently by properly choosing the driving phases. Moreover, the ground-state chiral currents for single- and two-qubit excitations are obtained and the Meissner-vortex phase transition is found. In the Meissner phase, the ground-state chiral current increases as the magnetic flux increases, while it decreases in the vortex phase. In addition, chiral dynamics, which depends crucially on the initial state of the system, is also revealed. Finally, the possible experimental observations of the chiral current and dynamics are addressed. Our results provide a new route to explore novel many-body properties induced by the interplay of the gauge field, two-leg hoppings, and interaction of photons on superconducting circuits.

DOI: [10.1103/PhysRevA.102.032610](https://doi.org/10.1103/PhysRevA.102.032610)**I. INTRODUCTION**

Due to their long coherence time, fine tunability, and high-precision measurement [1,2], superconducting circuits have emerged as a promising platform for processing quantum information [3,4] and quantum computing [5,6], as well as implementing quantum simulation [7,8]. The recent quantum-simulation experiments have attracted great attention in fundamental many-body physics [9], such as magnets [10,11], localizations [12,13], molecular energies [14], anionic braiding statistics [15,16], topological magnon insulators [17], strongly correlated quantum walks [18], and dissipatively stabilized Mott insulators [19] and quantum phase transitions [20]. Note that the observed many-body physics are mainly based on a chain of superconducting circuits. In a recent breakthrough experiment, two-leg superconducting circuits with 24 transmon qubits have been reported and single- and double-excitation dynamics observed [21]. This experiment opens a new route to explore exotic many-body physics [22–31], which can be induced by the competition between interleg and intraleg hoppings and strong interaction of photons on superconducting circuits.

On the other hand, the gauge field is essential for a wide range of research, from high-energy physics [32] and cosmology [33] to ultracold atoms [34–36] and condensed-matter physics [37]. Recently, the synthetic gauge field has attracted much attention for exploring exotic many-body quantum phenomena, such as the quantum Hall effect [38–40], the fractional quantum Hall effect [41–43], the fractal energy spectrum known as the Hofstadter’s butterfly [44–46], and the Meissner and vortex Mott insulator and superfluid [47–49]. In superconducting circuits, the synthetic gauge field was first proposed [50,51] and realized [52] in one unit cell by modulating the qubit couplings, and moreover, its induced chiral spin clusters have been achieved [53]. It is natural to ask the interesting question of how to achieve synthetic gauge fields in a two-leg superconducting qubit lattice with many unit cells. If realized, what interesting observable physics will occur?

In this paper, we present a feasible scheme to achieve the simulation of a synthetic gauge field on two-leg superconducting circuits. In contrast to the previous schemes [50–52], here we introduce an ac driving on each transmon qubit through the flux-bias line. More importantly, the realized synthetic magnetic flux per plaquette can be tuned independently by controlling the driving phases, which is better than the previous realizations in other quantum simulation systems, such as ultracold atoms [38,54–58], photonic [59–62], acoustics [63], and ion traps [64]. Based on the realized synthetic magnetic flux, the ground-state chiral current

\*guanxin810712@163.com

†zyxue83@163.com

‡chengang971@163.com

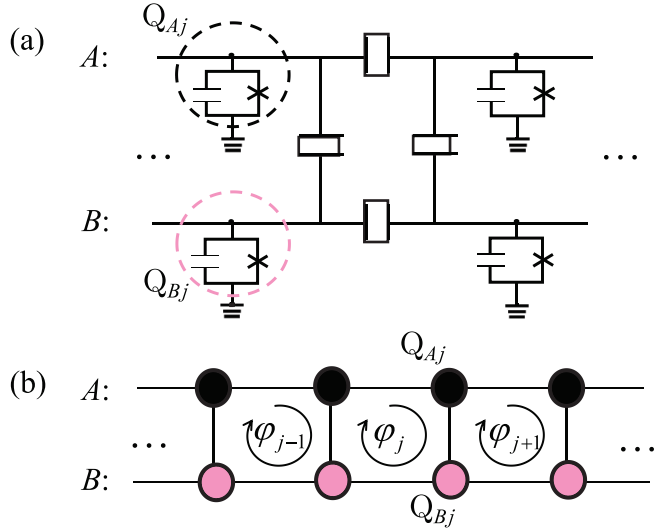


FIG. 1. Schematic of two-leg (labeled  $A$  and  $B$ , respectively) superconducting circuits with transmon qubits. All transmon qubits are coupled with their nearest-neighbor sites by capacitors. (a) Detailed illustration of the circuit of a unit plaquette.  $Q_{v,j}$  denotes the qubit at the  $j$ th site on the  $v$ th leg. (b) Schematic of the two-leg lattice with an effective magnetic flux per plaquette which can be controlled independently. Black and pink filled circles indicate the transmon qubits at the  $A$  and  $B$  legs, respectively.

with single- and two-qubit excitations are obtained and the Meissner-vortex quantum phase transition is also found. In the Meissner phase, the ground-state chiral current increases as the magnetic flux increases, while it decreases in the vortex phase. The chiral dynamics, which depends crucially on the initial state of the system, is also revealed. Finally, possible experimental observations of the chiral current and dynamics are also addressed. Our results provide a new way to explore rich many-body phenomena induced by the interplay of the gauge field, two-leg hoppings, and interaction of photons on superconducting circuits. Especially, based on the chiral property, photonic fractional topological insulators [65–67] and topological superfluids [68–70] can be explored, and high- $T_c$  superconductors in the underdoped regime can be simulated [71,72].

This paper is organized as follows. In Sec. II, we realize the synthetic gauge field tuned independently. In Secs. III and IV, we discuss the ground-state chiral current and chiral dynamics with single- and two-qubit excitations, respectively. In Sec. V, we present the possible experimental observations. The conclusions are given in Sec. VI.

## II. SYNTHETIC GAUGE FIELD

As shown in Fig. 1(a), we consider the same experimental setup about two-leg superconducting circuits with transmon qubits [21], whose dynamics is governed by a Bose-Hubbard ladder Hamiltonian,

$$\begin{aligned} \hat{H}_{\text{BH}} = & \sum_{v,j} \omega_{v,j}^0 \hat{a}_{v,j}^\dagger \hat{a}_{v,j} + \sum_{v,j} \frac{V_{v,j}}{2} \hat{n}_{v,j} (\hat{n}_{v,j} - 1) \\ & + \sum_{v,j} (g_{v,j} \hat{a}_{v(j-1)}^\dagger \hat{a}_{v,j} + \text{H.c.}) \\ & + \sum_j (\tilde{g}_j \hat{a}_{A,j}^\dagger \hat{a}_{B,j} + \text{H.c.}), \end{aligned} \quad (1)$$

where  $j$  is the number of the rung,  $v \in \{A, B\}$  labels the leg, the operator  $\hat{a}_{v,j}^\dagger$  ( $\hat{a}_{v,j}$ ) creates (annihilates) a photon at the  $j$ th site on the  $v$ th leg,  $\hat{n}_{v,j} = \hat{a}_{v,j}^\dagger \hat{a}_{v,j}$  is the number operator,  $\omega_{v,j}^0$  is the qubit frequency,  $V_{v,j}$  is the on-site attractive interaction at the  $j$ th site on the  $v$ th leg,  $g_{v,j}$  is the hopping strength between the nearest-neighbor sites along the leg  $v$ ,  $\tilde{g}_j$  is the interleg hopping strength at rung  $j$ , and H.c. is the Hermitian conjugate. In the experiment in [21], the transmon qubit has a strong anharmonicity,  $|V_{v,j}|/g_{v,j} \simeq 20$ , which allows that only one photon can be excited at each site. In this case, the nonlinear term of the Hamiltonian in Eq. (1) can be safely neglected.

To obtain the wanted synthetic gauge field, here we introduce an ac microwave driving in each transmon qubit, which is experimentally feasible through the flux-bias line [73]. In this case, each qubit frequency is modulated independently as

$$\omega_{v,j}(t) = \omega_{v,j}^0 + \varepsilon_{v,j} \sin(u_{v,j}t + \varphi_{v,j}), \quad (2)$$

where  $\varepsilon_{v,j}$ ,  $u_{v,j}$ , and  $\varphi_{v,j}$  are the driving amplitude, frequency, and phase, respectively. By applying the rotation frame with a unitary operator  $\hat{U} = \hat{U}_1 \times \hat{U}_2$ , where

$$\hat{U}_1 = \exp \left[ -i \sum_{v,j} \omega_{v,j}^0 \hat{n}_{v,j} t \right], \quad (3a)$$

$$\hat{U}_2 = \exp \left[ i \sum_{v,j} \hat{n}_{v,j} \alpha_{v,j} \cos(u_{v,j}t + \varphi_{v,j}) \right], \quad (3b)$$

with  $\alpha_{v,j} = \varepsilon_{v,j}/u_{v,j}$ , the transformed Hamiltonian

$$\hat{H}_t = \hat{U}^\dagger \hat{H}_{\text{BH}} \hat{U} + i \frac{d\hat{U}^\dagger}{dt} \hat{U} \quad (4)$$

can be divided into two parts as  $\hat{H}_t = \hat{H}_E + \hat{H}_{\text{AB}}$ , with

$$\begin{aligned} \hat{H}_E = & \sum_v g_{v1} \{ \hat{a}_{v1}^\dagger \hat{a}_{v2} e^{-i\Delta_{v2}t} \exp[-i\alpha_{v1} \cos(u_{v1}t + \varphi_{v1})] \exp[i\alpha_{v2} \cos(u_{v2}t + \varphi_{v2})] + \text{H.c.} \} \\ & + \sum_v g_{v2} \{ \hat{a}_{v2}^\dagger \hat{a}_{v3} e^{-i\Delta_{v3}t} \exp[-i\alpha_{v2} \cos(u_{v2}t + \varphi_{v2})] \exp[i\alpha_{v3} \cos(u_{v3}t + \varphi_{v3})] + \text{H.c.} \} + \dots, \end{aligned} \quad (5a)$$

$$\begin{aligned} \hat{H}_{\text{AB}} = & \tilde{g}_1 \{ \hat{a}_{A1}^\dagger \hat{a}_{B1} e^{-i\Delta_{AB1}t} \exp[-i\alpha_{A1} \cos(u_{A1}t + \varphi_{A1})] \exp[i\alpha_{B1} \cos(u_{B1}t + \varphi_{B1})] + \text{H.c.} \} \\ & + \tilde{g}_2 \{ \hat{a}_{A2}^\dagger \hat{a}_{B2} e^{-i\Delta_{AB2}t} \exp[-i\alpha_{A2} \cos(u_{A2}t + \varphi_{A2})] \exp[i\alpha_{B2} \cos(u_{B2}t + \varphi_{B2})] + \text{H.c.} \} + \dots, \end{aligned} \quad (5b)$$

with  $\Delta_{vj} = \omega_{vj}^0 - \omega_{v(j-1)}^0$  and  $\Delta_{ABj} = \omega_{Bj}^0 - \omega_{Aj}^0$ . Using the Jacobi-Anger identity,  $\exp[i\alpha \cos(ut + \varphi)] = \sum_{-\infty}^{\infty} i^m J_m(\alpha) \exp[im(ut + \varphi)]$ , where  $J_m(\alpha)$  is the  $m$ th Bessel function of the first kind, we have

$$\begin{aligned} \hat{H}_E &= \sum_{vj} g_{vj} \hat{a}_{v(j-1)}^\dagger \hat{a}_{vj} \sum_{m_1=-\infty}^{\infty} (-i)^{m_1} J_{m_1}(\alpha_{v(j-1)}) \exp[-im_1(u_{v(j-1)}t + \varphi_{v(j-1)})] \\ &\times \sum_{m_2=-\infty}^{\infty} i^{m_2} J_{m_2}(\alpha_{vj}) \exp[i(m_2 u_{vj} - \Delta_{vj})t + m_2 \varphi_{vj}] + \text{H.c.}, \end{aligned} \quad (6a)$$

$$\begin{aligned} \hat{H}_{AB} &= \sum_j \tilde{g}_j \hat{a}_{Aj}^\dagger \hat{a}_{Bj} \sum_{m_1=-\infty}^{\infty} (-i)^{m_1} J_{m_1}(\alpha_{Aj}) \exp[-im_1(u_{Aj}t + \varphi_{Aj})] \\ &\times \sum_{m_2=-\infty}^{\infty} i^{m_2} J_{m_2}(\alpha_{Bj}) \exp[i(m_2 u_{Bj} - \Delta_{ABj})t + m_2 \varphi_{Bj}] + \text{H.c.} \end{aligned} \quad (6b)$$

When choosing  $\Delta_{vj} = u_{vj} (-u_{vj})$  for odd (even)  $j$  and  $\Delta_{ABj} = u_{Bj}$ , and considering the case where  $u_{vj} \gg \{g_{vj}, \tilde{g}_j\}$ , the oscillating terms in Eqs. (6a) and (6b) are neglected by applying the rotating-wave approximation. Finally, the effective Hamiltonian is given by

$$\begin{aligned} \hat{H} &= \sum_{vj} (t_{vj} e^{i\tilde{\varphi}_{vj}} \hat{a}_{v(j-1)}^\dagger \hat{a}_{vj} + \text{H.c.}) \\ &+ \sum_j (\tilde{t}_j e^{i\tilde{\varphi}'_{Bj}} \hat{a}_{Aj}^\dagger \hat{a}_{Bj} + \text{H.c.}), \end{aligned} \quad (7)$$

where  $t_{vj} = g_{vj} J_0(\alpha_{v(j-1)}) J_1(\alpha_{vj})$ ,  $\tilde{t}_j = \tilde{g}_j J_0(\alpha_{Aj}) J_1(\alpha_{Bj})$ ,  $\tilde{\varphi}_{vj} = (-1)^{j+1} \varphi_{vj} + \pi/2$ , and  $\tilde{\varphi}'_{Bj} = \varphi_{Bj} + \pi/2$ .

The Hamiltonian in Eq. (7) shows clearly that the driving phase  $\tilde{\varphi}_{vj}$  leads to a complex hopping between any two nearest-neighbor sites and thus causes each plaquette to accumulate a gauge-invariant magnetic flux  $\varphi_j = \tilde{\varphi}_{Aj} + \tilde{\varphi}'_{Bj} - \tilde{\varphi}_{Bj} - \tilde{\varphi}'_{v(j-1)}$  [see Fig. 1(b)]. This synthetic magnetic flux per plaquette can be tuned independently by choosing the driving phases in the transmon qubits, which is better than the previous realizations in other systems. If  $\varphi_j = \varphi$  is chosen, a uniform flux is formed [48,57,74]; if  $\varphi_j = (-1)^j \varphi$ , a staggered flux is generated [54,75–78]; and if  $\varphi_j = j\varphi$ , a site-dependent flux is achieved [38,55,56,59].

### III. GROUND-STATE CHIRAL CURRENT

The synthetic magnetic flux achieved can generate rich quantum phenomena. As an example, we investigate the experimentally measurable ground-state chiral current and chiral dynamics of the ladder system. For simplicity, we set  $\alpha_{vj} = \alpha$  and  $g_{vj} = \tilde{g}_j = g$ , which means that  $t_{vj} = \tilde{t}_j = t_0 = g J_0(\alpha) J_1(\alpha)$ . The driving phases are taken as  $\tilde{\varphi}_{Aj} - \tilde{\varphi}_{Bj} = \tilde{\varphi}'_{Bj} - \tilde{\varphi}'_{v(j-1)} = \varphi/2$ , and the synthetic magnetic flux thus becomes  $\varphi_j = \varphi$ . In this section, we mainly discuss the ground-state chiral current. The case of single-qubit excitation is first considered and the case of two-qubit excitation is then addressed briefly.

By performing the Fourier transformation  $\hat{a}_{vk} = \sum_j e^{ikj} \hat{a}_{vj} / \sqrt{N}$ , where  $N$  is the number of ladder rungs, the Hamiltonian in Eq. (7) becomes  $\hat{H} = \sum_k (\hat{a}_{Ak}^\dagger, \hat{a}_{Bk}^\dagger) \hat{h}(k) \begin{pmatrix} \hat{a}_{Ak} \\ \hat{a}_{Bk} \end{pmatrix}$ ,

where

$$\hat{h}(k) = \varepsilon_0(k) \hat{I} + t_0 \hat{\sigma}_x + \varepsilon_z(k) \hat{\sigma}_z \quad (8)$$

and  $\hat{I}$  is the identity operator,  $\hat{\sigma}_x$  and  $\hat{\sigma}_z$  are the Pauli spin operators in the  $x$  and  $z$  directions,  $\varepsilon_0(k) = 2t_0 \cos(\varphi/2) \cos k$ , and  $\varepsilon_z(k) = 2t_0 \sin(\varphi/2) \sin k$ . Since legs  $A$  and  $B$  act, respectively, as the spin-up and spin-down components, the  $\hat{\sigma}_x$  term governs the tunneling between two legs. The  $\hat{\sigma}_z$  term, determined by the nonzero magnetic flux  $\varphi$ , generates spin-momentum locking so that the spin-up and spin-down photons minimize their energies by having positive and negative momenta, respectively. The Hamiltonian in Eq. (8) exhibits time-reversal invariance [74], which leads to Kramers degeneracy of the ground state, as shown below.

With the diagonalization of the momentum-space Hamiltonian in Eq. (8), we obtain two energy bands,

$$E(k) = \varepsilon_0(k) \pm \sqrt{\varepsilon_z(k)^2 + t_0^2}, \quad (9)$$

which are plotted, in Fig. 2, as functions of the momentum  $k$  for  $\varphi = 0.1\pi$  [Fig. 2(a)] and  $\varphi = 0.9\pi$  [Fig. 2(b)]. For small  $\varphi$ , the lower energy band only has one minimum, at  $k = \pi$  or  $k = -\pi$ , as shown in Fig. 2(a). With increasing  $\varphi$ , two Kramers degeneracy points occur, at  $k = \pm q$ , with

$$q = \frac{1}{2} \arccos \left\{ \frac{1 + \cos(\varphi)}{2[1 - \cos(\varphi)]} + \cos(\varphi) \right\}, \quad (10)$$

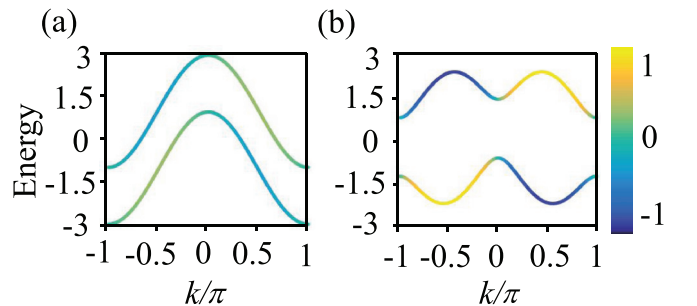


FIG. 2. Energy bands as functions of the momentum  $k$  for (a)  $\varphi = 0.1\pi$  and (b)  $\varphi = 0.9\pi$ . The color indicates the value of  $\langle \hat{\sigma}_z \rangle_k$ . Here  $t_0$  is used as the unit.

as shown in Fig. 2(b). The critical point where the lower energy band changes from one minimum to two minima is given by  $\varphi_c = 2 \arccos(\sqrt{17/4} - 1/4)$ . For simplicity, here we choose  $\varphi \in (0, \pi)$ .

With single-qubit excitation, the eigenfunction of the lower energy band is obtained by

$$|\psi_{Lk}\rangle = (\alpha_{Lk}\hat{a}_{kA}^\dagger + \beta_{Lk}\hat{a}_{kB}^\dagger)|0\rangle, \quad (11)$$

where  $|0\rangle$  is the vacuum state,

$$\alpha_{Lk} = \frac{(\bar{\varepsilon}_z - \sqrt{1 + \bar{\varepsilon}_z^2})}{\sqrt{[(\bar{\varepsilon}_z - \sqrt{1 + \bar{\varepsilon}_z^2})^2 + 1]}}, \quad (12a)$$

$$\beta_{Lk} = \frac{1}{\sqrt{[(\bar{\varepsilon}_z - \sqrt{1 + \bar{\varepsilon}_z^2})^2 + 1]}}, \quad (12b)$$

with  $\bar{\varepsilon}_z = 2 \sin(\varphi/2) \sin k$ . In terms of Eq. (11), we have

$$\langle \hat{\sigma}_z \rangle_{Lk} = \frac{(\bar{\varepsilon}_z - \sqrt{1 + \bar{\varepsilon}_z^2})^2 - 1}{(\bar{\varepsilon}_z - \sqrt{1 + \bar{\varepsilon}_z^2})^2 + 1}. \quad (13)$$

Equation (13) shows clearly that when  $k > 0$  (i.e.,  $\bar{\varepsilon}_z > 0$ ),  $\langle \hat{\sigma}_z \rangle_{Lk} < 0$ , and vice versa, which indicates the spin-momentum locking effect induced by the nonzero magnetic flux. When  $\varphi = 0$ ,  $\langle \hat{\sigma}_z \rangle_{Lk} \equiv 0$  for any  $k$ .

Due to the spin-momentum locking, the photons in the  $A$  leg move towards the left, whereas the photons in the  $B$  leg move towards the right. As a result, the ladder system with nonzero magnetic flux exhibits a chiral current defined as

$$\hat{J}_C = \hat{J}_A - \hat{J}_B, \quad (14)$$

with  $\hat{J}_A = \sum_j \hat{J}_{A_j}$  and  $\hat{J}_B = \sum_j \hat{J}_{B_j}$ , where

$$\hat{J}_{A_j} = it_0 e^{i\frac{\varphi}{2}} \hat{a}_{A_j}^\dagger \hat{a}_{A_{(j+1)}} + \text{H.c.}, \quad (15a)$$

$$\hat{J}_{B_j} = it_0 e^{-i\frac{\varphi}{2}} \hat{a}_{B_j}^\dagger \hat{a}_{B_{(j+1)}} + \text{H.c.} \quad (15b)$$

On the other hand, since the  $\hat{\sigma}_x$  term in the Hamiltonian in Eq. (8) governs the tunneling between the two legs, it is necessary to define the current at rung  $j$  as

$$\hat{J}_j = it_0 \hat{a}_{A_j}^\dagger \hat{a}_{B_j} + \text{H.c.} \quad (16)$$

In terms of Eqs. (14)–(16), we can investigate the ground-state current of the Hamiltonian in Eq. (7). For  $\varphi < \varphi_c$ , i.e., when the lower energy band has one minimum, the ground-state wave function  $|\psi_G\rangle = |\psi_{L\pi}\rangle$ , whose corresponding currents are calculated as

$$\langle \hat{J}_{A_j} \rangle_{L\pi} = -\langle \hat{J}_{B_j} \rangle_{L\pi} = \frac{t_0}{N} \sin\left(\frac{\varphi}{2}\right), \quad (17a)$$

$$\langle \hat{J}_C \rangle_{L\pi} = 2t_0 \sin\left(\frac{\varphi}{2}\right), \quad (17b)$$

$$\langle \hat{J}_j \rangle_{L\pi} = 0. \quad (17c)$$

These equations show that the currents along the  $A$  and  $B$  legs have opposite directions but with the same magnitudes, i.e., a nonzero chiral current is generated, while the current at rung  $j$  vanishes. This phenomenon clearly characterizes the Meissner effect [79].

For  $\varphi > \varphi_c$ , i.e., the lower energy band has two minima, the ground-state wave function becomes  $|\psi_G\rangle =$

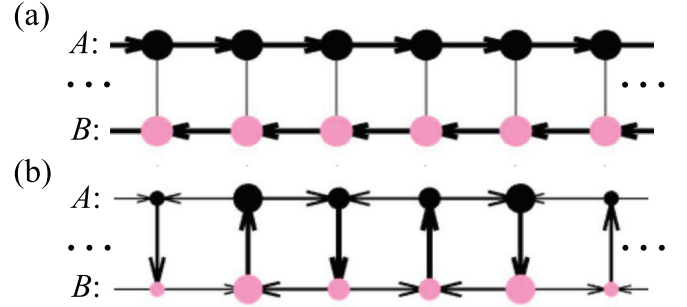


FIG. 3. Currents between neighboring sites for (a)  $\varphi = 0.1\pi$  and (b)  $\varphi = 0.9\pi$  when  $N = 50$ . The thicknesses of the arrows indicate their strengths. The sizes of the black and pink filled circles denote the local densities at rungs on the  $A$  and  $B$  legs, respectively. Here  $t_0$  is used as the unit.

$(|\psi_{L(-q)}\rangle + |\psi_{Lq}\rangle)/\sqrt{2}$ . In this case, the ground-state currents are given by

$$\langle \hat{J}_{A_j} \rangle_{Lq} = \frac{t_0}{N} \left[ \alpha_{L(-q)}^2 \sin\left(q - \frac{\varphi}{2}\right) - \alpha_{Lq}^2 \sin\left(q + \frac{\varphi}{2}\right) - 2\alpha_{L(-q)}\alpha_{Lq} \sin\left(\frac{\varphi}{2}\right) \cos(q + 2qj) \right], \quad (18a)$$

$$\langle \hat{J}_{B_j} \rangle_{Lq} = \frac{t_0}{N} \left[ \beta_{L(-q)}^2 \sin\left(q + \frac{\varphi}{2}\right) - \beta_{Lq}^2 \sin\left(q - \frac{\varphi}{2}\right) + 2\beta_{L(-q)}\beta_{Lq} \sin\left(\frac{\varphi}{2}\right) \cos(q + 2qj) \right], \quad (18b)$$

$$\langle \hat{J}_C \rangle_{Lq} = t_0 \left[ \alpha_{Lq}^2 \sin\left(\frac{\varphi}{2} + q\right) - \alpha_{L(-q)}^2 \sin\left(q - \frac{\varphi}{2}\right) - \beta_{Lq}^2 \sin\left(q - \frac{\varphi}{2}\right) + \beta_{L(-q)}^2 \sin\left(\frac{\varphi}{2} + q\right) \right], \quad (18c)$$

$$\langle \hat{J}_j \rangle_{Lq} = \frac{t_0}{N} \sin(2qj) [\alpha_{Lq}\beta_{L(-q)} - \alpha_{L(-q)}\beta_{Lq}]. \quad (18d)$$

Since  $\alpha_{L(-q)} = -\beta_{Lq}$  and  $\alpha_{Lq} = -\beta_{L(-q)}$ , it is easy to verify that  $\langle \hat{J}_{A_j} \rangle_{Lq} = -\langle \hat{J}_{B_j} \rangle_{Lq}$ . Equations (18a), (18b), and (18d) show that the currents between any two nearest-neighbor sites vary periodically with increasing  $j$ , characterizing the vortex current [80].

In Fig. 3, we plot the currents between any two nearest-neighbor sites for  $\varphi = 0.1\pi$  [Fig. 3(a)] and  $\varphi = 0.9\pi$  [Fig. 3(b)], which support the above analytical results. In Fig. 4(a), we plot the ground-state chiral current as a function of  $\varphi$ . With increasing  $\varphi$ , this chiral current first increases to a maximal value at the critical point  $\varphi_c$  and then decreases, which characterizes a transition from the Meissner phase to the vortex phase [48,78]. For a finite size, this transition feature remains but the critical point changes slightly, which means that the Meissner and vortex phases as well as their transition can be observed in the current experimental setup. In Fig. 4(b), we plot the ground-state chiral current for two-qubit excitation, which has properties similar to those for single-qubit excitation.

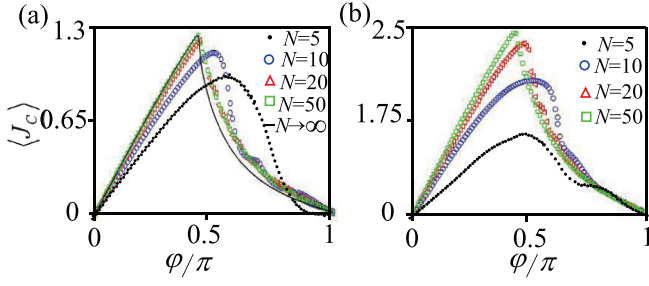


FIG. 4. Ground-state chiral currents as functions of  $\varphi$  for (a) single-qubit and (b) two-qubit excitation. The solid line in (a) is the analytical result from Eq. (18c). Black dots, open blue circles, open red triangles, and open green squares are the results for  $N = 5, 10, 20,$  and  $50,$  respectively. Here  $t_0$  is used as the unit.

#### IV. CHIRAL DYNAMICS

We now investigate the chiral dynamics of the Hamiltonian in Eq. (7) with  $N = 10$  and  $\varphi = 0.5\pi$ . For simplicity, we set  $t_0 = 1$  in the following discussion. We first consider the case of single-qubit excitation, denoted  $\hat{a}_{vj}^\dagger|0\rangle$ , which describes that the qubit at the  $j$ th site on the  $v$ th leg is excited. In Fig. 5, we plot the density distributions of photons at each site on the ladder at times  $t = 0$  and  $t = 1$ , when the initial states are prepared, respectively, as  $|\psi(0)\rangle_{1S} = (\hat{a}_{A5}^\dagger + \hat{a}_{B5}^\dagger)|0\rangle/\sqrt{2}$  ( $a_1, a_2$ ),  $|\psi(0)\rangle_{1AS} = (\hat{a}_{A5}^\dagger - \hat{a}_{B5}^\dagger)|0\rangle/\sqrt{2}$  ( $b_1, b_2$ ), and  $|\psi(0)\rangle_{1E} = \hat{a}_{B5}^\dagger|0\rangle$  ( $c_1, c_2$ ). This figure shows that for the initial state  $|\psi(0)\rangle_{1S}$ , most photons move to the left (right) of the central rung on the  $A$ ( $B$ ) leg [see Fig. 5(a<sub>2</sub>)], which characterizes chiral dynamics. The converse occurs for the initial state  $|\psi(0)\rangle_{1AS}$  [see Fig. 5(b<sub>2</sub>)], while for the initial state  $|\psi(0)\rangle_{1E}$ , the photons simultaneously move to both sides of the central rung [see Fig. 5(c<sub>2</sub>)], i.e., the chiral dynamics disappears. In order to see these results clearly, we consider a

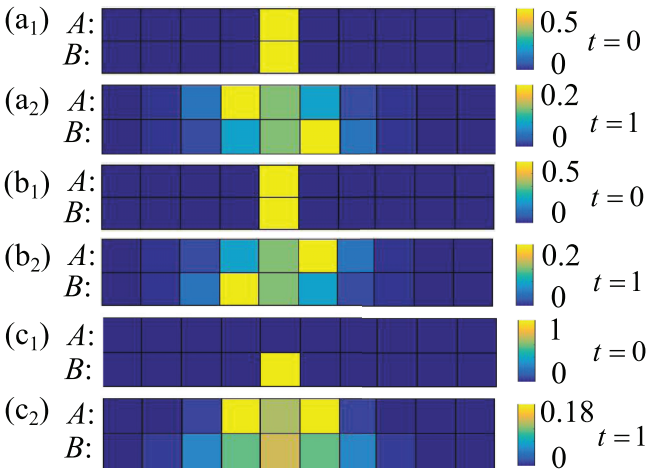


FIG. 5. Density distributions of photons at each site with single-qubit excitation for the initial states  $|\psi(0)\rangle_{1S} = (\hat{a}_{A5}^\dagger + \hat{a}_{B5}^\dagger)|0\rangle/\sqrt{2}$  with (a<sub>1</sub>)  $t = 0$  and (a<sub>2</sub>)  $t = 1$ ,  $|\psi(0)\rangle_{1AS} = (\hat{a}_{A5}^\dagger - \hat{a}_{B5}^\dagger)|0\rangle/\sqrt{2}$  with (b<sub>1</sub>)  $t = 0$  and (b<sub>2</sub>)  $t = 1$ , and  $|\psi(0)\rangle_{1E} = \hat{a}_{B5}^\dagger|0\rangle$  with (c<sub>1</sub>)  $t = 0$  and (c<sub>2</sub>)  $t = 1$ . In all figures, the synthetic magnetic flux  $\varphi = 0.5\pi$ . Here  $1/t_0$  is used as the unit.

short-time ( $\delta t$ ) dynamics, in which the time-dependent wave function is obtained, up to second order, as  $|\psi(\delta t)\rangle \simeq [1 - i\hat{H}\delta t - (\hat{H}\delta t)^2/2]|\psi(0)\rangle$ . As a result, the differences between the photons moving to the right and left of the center rung on the  $A$  and  $B$  legs under these three initial states are given, respectively, by

$$\langle \Delta \hat{n}_A \rangle_{1S} = -\langle \Delta \hat{n}_B \rangle_{1S} = \delta t^3 \sin(\varphi), \quad (19a)$$

$$\langle \Delta \hat{n}_A \rangle_{1AS} = -\langle \Delta \hat{n}_B \rangle_{1AS} = -\delta t^3 \sin(\varphi), \quad (19b)$$

$$\langle \Delta \hat{n}_A \rangle_{1E} = \langle \Delta \hat{n}_B \rangle_{1E} = 0, \quad (19c)$$

where  $\Delta \hat{n}_A = \sum_{j=1}^4 \hat{n}_{Aj} - \sum_{j=6}^{10} \hat{n}_{Aj}$  and  $\Delta \hat{n}_B = \sum_{j=1}^4 \hat{n}_{Bj} - \sum_{j=6}^{10} \hat{n}_{Bj}$ . Equations (19a) and (19b) show clearly that for the initial states  $|\psi(0)\rangle_{1S}$  and  $|\psi(0)\rangle_{1AS}$ , the opposite differences are raised by nonzero  $\varphi$ , and chiral dynamics can thus be formed. However, for the initial state  $|\psi(0)\rangle_{1E}$ , both differences disappear [see Eq. (19c)], i.e., no chiral dynamics occurs.

These results can be understood by considering the properties of both energy bands shown in Fig. 2. The fundamental information on the lower band has been given in the previous section. The eigenfunction of the upper energy band is given by

$$|\psi_{Uk}\rangle = (\alpha_{Uk} \hat{a}_{kA}^\dagger + \beta_{Uk} \hat{a}_{kB}^\dagger)|0\rangle, \quad (20)$$

where

$$\alpha_{Uk} = \frac{(\bar{\varepsilon}_z + \sqrt{1 + \bar{\varepsilon}_z^2})}{\sqrt{[(\bar{\varepsilon}_z + \sqrt{1 + \bar{\varepsilon}_z^2})^2 + 1]}}, \quad (21a)$$

$$\beta_{Uk} = \frac{1}{\sqrt{[(\bar{\varepsilon}_z + \sqrt{1 + \bar{\varepsilon}_z^2})^2 + 1]}}. \quad (21b)$$

From Eqs. (11) and (20), we obtain

$$\hat{a}_{Ak}^\dagger|0\rangle = -\alpha_{L(-k)}|\psi_{Uk}\rangle + \alpha_{Lk}|\psi_{Lk}\rangle, \quad (22a)$$

$$\hat{a}_{Bk}^\dagger|0\rangle = -\alpha_{L(-k)}|\psi_{Uk}\rangle - \alpha_{Lk}|\psi_{Lk}\rangle, \quad (22b)$$

where the relations  $\alpha_{Uk} = \beta_{Lk}$ ,  $\beta_{Uk} = -\alpha_{Lk}$ , and  $\alpha_{L(-k)} = -\beta_{Lk}$  have been used. In terms of Eqs. (22a) and (22b), the three initial states we have chosen are rewritten as

$$|\psi(0)\rangle_{1S} = -\sum_k \sqrt{2} e^{i5k} \alpha_{L(-k)} |\psi_{Uk}\rangle, \quad (23a)$$

$$|\psi(0)\rangle_{1AS} = -\sum_k \sqrt{2} e^{i5k} \alpha_{Lk} |\psi_{Lk}\rangle, \quad (23b)$$

$$|\psi(0)\rangle_{1E} = \sum_k e^{i5k} (\alpha_{L(-k)} |\psi_{Uk}\rangle + \alpha_{Lk} |\psi_{Lk}\rangle). \quad (23c)$$

Equations (23a) and (23b) show clearly that for the symmetric (antisymmetric) initial state  $|\psi(0)\rangle_{1S}$  ( $|\psi(0)\rangle_{1AS}$ ), the photons only populate the upper (lower) band. Due to the spin-momentum locking effect in the two bands, chiral dynamics occurs. Equation (23c) shows that when the initial state is chosen as  $|\psi(0)\rangle_{1E}$ , the photons populate equally the upper and lower bands with opposite  $k$ . Since the two energy bands have opposite chirality (see Fig. 2), the photons move to the

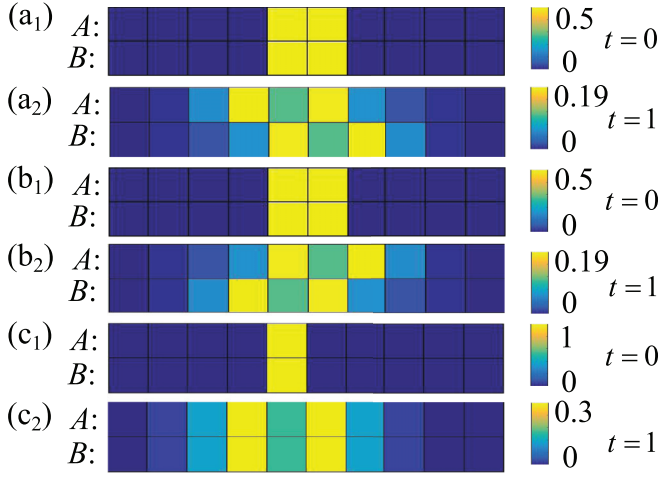


FIG. 6. Density distributions of photons at each site with two-qubit excitation for the initial states  $|\psi(0)\rangle_{2S} = (\hat{a}_{A5}^\dagger + \hat{a}_{B5}^\dagger)(\hat{a}_{A6}^\dagger + \hat{a}_{B6}^\dagger)|0\rangle/2$  with (a<sub>1</sub>)  $t = 0$  and (a<sub>2</sub>)  $t = 1$ ,  $|\psi(0)\rangle_{2AS} = (\hat{a}_{A5}^\dagger - \hat{a}_{B5}^\dagger)(\hat{a}_{A6}^\dagger - \hat{a}_{B6}^\dagger)|0\rangle/2$  with (b<sub>1</sub>)  $t = 0$  and (b<sub>2</sub>)  $t = 1$ , and  $|\psi(0)\rangle_{2E} = \hat{a}_{A5}^\dagger \hat{a}_{B5}^\dagger |0\rangle$  with (c<sub>1</sub>)  $t = 0$  and (c<sub>2</sub>)  $t = 1$ . In all figures, the synthetic magnetic flux  $\varphi = 0.5\pi$ . Here  $1/t_0$  is used as the unit.

both sides of their initial positions simultaneously and the chiral dynamics thus disappears.

In Fig. 6, we plot the density distributions of photons at times  $t = 0$  and  $t = 1$  for two-qubit excitation of  $\hat{a}_{\nu j}^\dagger \hat{a}_{\nu' j'}^\dagger |0\rangle$ , which describes that the qubits at the  $j$ th site on the  $\nu$ th leg and at the  $j'$ th site on the  $\nu'$ th leg are excited. We emphasize that  $\nu$  and  $\nu'$ , and  $j$  and  $j'$ , are not equal simultaneously. The initial states are chosen, respectively, as  $|\psi(0)\rangle_{2S} = (\hat{a}_{A5}^\dagger + \hat{a}_{B5}^\dagger)(\hat{a}_{A6}^\dagger + \hat{a}_{B6}^\dagger)|0\rangle/2$  [Figs. 6(a<sub>1</sub>) and 6(a<sub>2</sub>)],  $|\psi(0)\rangle_{2AS} = (\hat{a}_{A5}^\dagger - \hat{a}_{B5}^\dagger)(\hat{a}_{A6}^\dagger - \hat{a}_{B6}^\dagger)|0\rangle/2$  [Figs. 6(b<sub>1</sub>) and 6(b<sub>2</sub>)], and  $|\psi(0)\rangle_{2E} = \hat{a}_{A5}^\dagger \hat{a}_{B5}^\dagger |0\rangle$  [Figs. 6(c<sub>1</sub>) and 6(c<sub>2</sub>)]. This figure shows conclusions similar to those obtained with single-qubit excitation, i.e., for the initial states  $|\psi(0)\rangle_{2S}$  and  $|\psi(0)\rangle_{2AS}$ , the system has opposite chiral dynamics, which disappears for the initial state  $|\psi(0)\rangle_{2E}$ .

## V. POSSIBLE EXPERIMENTAL OBSERVATION

In this section, we briefly discuss how to detect the ground-state chiral current and the chiral dynamics in experiments. Note that the ground state  $|\psi_G\rangle$  of the effective Hamiltonian in Eq. (7) is obtained in the rotating frame, it should first be prepared based on a given initial state  $|\psi(0)\rangle_L$  of the Hamiltonian in Eq. (1) in the laboratory frame. The basic method is similar to that of the recent experiment [52]. As an example, we first consider the case of single-qubit excitation with  $|\psi(0)\rangle_L = |1\rangle_{\nu j} \otimes \prod_{\nu' j' \neq \nu j} |0\rangle_{\nu' j'}$ . According to the evolution generated by the Hamiltonian in Eq. (1), a prerotation state is realized in the same frame as  $|P\rangle_L = \prod_{\nu j} |\psi\rangle_{\nu j}$  with  $|\psi\rangle_{\nu j} = \cos(\theta_{\nu j}^P/2)|0\rangle_{\nu j} + e^{i\chi_{\nu j}^P} \sin(\theta_{\nu j}^P/2)|1\rangle_{\nu j}$ , where  $\theta_{\nu j}^P = 2 \arccos(\sqrt{1 - |\lambda_{\nu j}^P|^2})$  ( $\chi_{\nu j}^P = -i \ln[\lambda_{\nu j}^P / \sin(\theta_{\nu j}^P/2)]$ ) denotes the angle between state  $|\psi\rangle_{\nu j}$  and the  $z$  ( $x$ ) axis in the Bloch sphere. In the above equation,  $\lambda_{\nu j}^P$  is the amplitude of the

single-qubit excitation component in the prerotation state. Then the ground state  $|\psi_G\rangle$  is prepared by driving the rotations of each qubit in the Bloch sphere via microwave pulses [3,81–85]. Since the ground state has the same form as the pre-rotation state  $|P\rangle_L$ , but only a different amplitude  $\lambda_{\nu j}^G$ , the rotation operator is given by  $U_R = \exp[i(\theta_{\nu j}^G - \theta_{\nu j}^P)\hat{\sigma}_z + i(\chi_{\nu j}^G - \chi_{\nu j}^P)\hat{\sigma}_x]$ . It should be emphasized that the specific values of  $\lambda_{\nu j}^P$  and  $\lambda_{\nu j}^G$  should be calculated numerically based on the experimental parameters. In the case of two-qubit excitation, the initial state should be chosen as  $|\psi(0)\rangle_L = |1\rangle_{\nu j} \otimes |1\rangle_{\nu' j' \neq \nu j} \otimes \prod_{\nu'' j'' \neq \nu j \neq \nu' j'} |0\rangle_{\nu'' j''}$ . The explicit forms of states  $|P\rangle_L$  and  $|\psi_G\rangle$  in this case are the same as those with single-qubit excitation. This means that the corresponding amplitude  $\lambda_{\nu j}^G$  ( $\lambda_{\nu j}^P$ ) of the two-qubit excitation component in state  $|\psi_G\rangle$  ( $|P\rangle_L$ ) can also be calculated, and  $\theta_{\nu j}^G$  ( $\theta_{\nu j}^P$ ) and  $\chi_{\nu j}^G$  ( $\chi_{\nu j}^P$ ) can thus be solved. Finally, after applying the rotation operator  $U_R$ , the ground state  $|\psi_G\rangle$  for two-qubit excitation can also be prepared.

After preparing the ground state  $|\psi_G\rangle$  and based on the state tomography that has been developed successfully [86], the density of the states at each site can be measured and the matrix density  $\hat{\rho}$  is thus constructed. This indicates that the ground-state chiral current can be obtained by  $\langle \hat{J}_C \rangle = \text{tr}(\hat{\rho} \hat{J}_C)$  [52], where  $\text{tr}$  is the trace operator. If the ground-state chiral current increases (decreases) as the magnetic flux increases, the Meissner (vortex) phase is found. It should be noted that the scalability of this measuring method should be addressed since fully describing the  $2N$ -qubit system requires a density matrix with  $2^{4N}$  elements. Therefore, it is very expensive for a large number of qubits. However, in our system, the ground-state chiral current can be observed when  $N = 5$  (i.e., 10 qubits), as shown by the black dots in Fig. 4. In this case, full tomography measurement requires  $3^{10}$  tomographic operations and  $2^{10}$  probabilities for each operation, allowing us to reconstruct all elements of the density matrix. This has been realized in the current experiment, which takes about 40 h [87]. With increasing  $N$ , the measurements and computational resources increase exponentially. Realizing quantum-state tomography with more qubits might be possible by applying some additional techniques, such as two-body reduced density matrices [88], compressed sensing [89,90], machine learning [91–93], matrix product states [94], and parameterized quantum circuits [95,96].

To observe chiral dynamics, preparing the corresponding initial states plays a crucial role. The initial state  $\hat{a}_{B5}^\dagger |0\rangle$  ( $\hat{a}_{A5}^\dagger \hat{a}_{B5}^\dagger |0\rangle$ ) can be prepared directly by microwave driving. For the superposition state  $(\hat{a}_{A5}^\dagger + \hat{a}_{B5}^\dagger) |0\rangle / \sqrt{2}$  [ $(\hat{a}_{A5}^\dagger - \hat{a}_{B5}^\dagger) |0\rangle / \sqrt{2}$ ], we first turn off all the phases and the hopping strengths between the  $\nu 5$  site and its nearest-neighbor sites and prepare the system in state  $\hat{a}_{\nu 5}^\dagger |0\rangle$ . Since the superposition state  $(\hat{a}_{A5}^\dagger + \hat{a}_{B5}^\dagger) |0\rangle / \sqrt{2}$  [ $(\hat{a}_{A5}^\dagger - \hat{a}_{B5}^\dagger) |0\rangle / \sqrt{2}$ ] is the ground state of the isolate rung subsystem at  $j = 5$  with the negative [positive] interleg hopping strength, we adiabatically turn on the interleg hopping strength towards the negative [positive] by tuning the parameters  $\alpha_{A5}$  and  $\alpha_{B5}$  (see Fig. 7). As a result, the required superposition states are prepared. Similarly, in the case of two-qubit excitation, the initial superposition state  $(\hat{a}_{A5}^\dagger + \hat{a}_{B5}^\dagger)(\hat{a}_{A6}^\dagger + \hat{a}_{B6}^\dagger) |0\rangle / 2$  [ $(\hat{a}_{A5}^\dagger - \hat{a}_{B5}^\dagger)(\hat{a}_{A6}^\dagger - \hat{a}_{B6}^\dagger) |0\rangle / 2$ ] is the ground state of the subsystem for two isolate rungs at

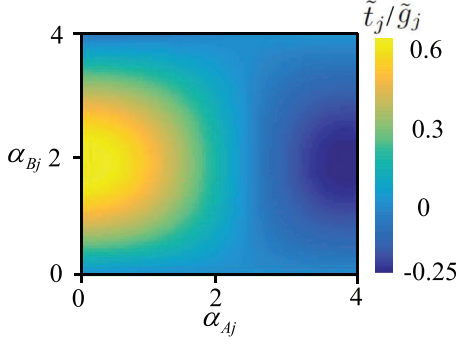


FIG. 7. Interleg hopping strength as a function of the parameters  $\alpha_{A_j}$  and  $\alpha_{B_j}$ .

$j = 5$  and  $j = 6$  with a negative [positive] interleg hopping strength. We first turn off all the phases and hopping strengths between the  $v_j$  ( $j = 5$  and  $j = 6$ ) site and its nearest-neighbor sites and drive the system in state  $\hat{a}_{A5}^\dagger \hat{a}_{A6}^\dagger |0\rangle$ . The required superposition states can be prepared by adiabatically turning on the interleg hopping strengths at both the fifth and the sixth rungs via the parameters  $\alpha_{A5}$ ,  $\alpha_{B5}$ ,  $\alpha_{A6}$ , and  $\alpha_{B6}$  (see Fig. 7). Then chiral dynamics can be observed by detecting the excitation number  $\hat{n}_{v,j}(t)$  of each qubit, which has been realized in experiments [18,21]. To observe the chirality in Figs. 5 and 6, we only need to detect the excitation numbers of the qubits at the fourth, fifth, sixth, and seventh rungs, as shown in Fig. 8. In the case of single-qubit excitation, with increasing  $t$ , the excitation number from the fifth rung propagating to the fourth (sixth) rung is larger than that propagating to the sixth (fourth) rung on leg A with the initial state  $|\psi\rangle_{1S}$  ( $|\psi\rangle_{1AS}$ ) [see Figs. 8(a<sub>1</sub>) and 8(b<sub>1</sub>)]. The propagation on leg B is opposite [see Figs. 8(a<sub>2</sub>) and 8(b<sub>2</sub>)], which characterizes the chiral dynamics. With initial state  $|\psi\rangle_{1E}$ , the excitation numbers from the fifth rung propagating to the fourth and sixth rungs are equal on both leg A and leg B [see Figs. 8(c<sub>1</sub>) and 8(c<sub>2</sub>)], which indicates the disappearance of the chirality. The chirality in the case of two-qubit excitation can also be observed similarly, as shown in Figs. 8(d<sub>1</sub>)–8(f<sub>2</sub>). In fact, when the qubit states' readout signals are amplified by Josephson parametric, high-electron-mobility transistor, and microwave amplifiers, the dynamics of each qubit can be extracted by and analog-to-digital converter [21].

Finally, we discuss the feasibility under the current experimental parameters [21,73]. The hopping strengths  $g_{vj}$  and  $\tilde{g}_j$  of the Hamiltonian in Eq. (1) are about  $2\pi \times 10$  MHz [21], and the driving amplitude  $\varepsilon_{vj}$  and frequency  $u_{vj}$  of the external flux can be controlled from  $2\pi \times 20$  to  $2\pi \times 220$  MHz [73]. When tuning  $u_{vj}$  from  $2\pi \times 100$  to  $2\pi \times 220$  MHz, the condition  $u_{vj} \gg \{g_{vj}, \tilde{g}_j\}$ , which plays a crucial role in deriving the Hamiltonian in Eq. (7), can be well satisfied. In addition, by properly choosing the driving amplitude and frequency, the parameter  $\alpha_{vj} = \varepsilon_{vj}/u_{vj}$  can be tuned from 0.1 to 2, and thus  $\tilde{t}_j = t_0 = \tilde{g}_j J_0(\alpha_{A_j}) J_1(\alpha_{B_j})$  ranges from  $0.2\tilde{g}_j$  to  $0.6\tilde{g}_j$ , as shown in Fig. 7. If we choose  $\tilde{t}_j = 0.6\tilde{g}_j$ , the chiral dynamics plotted in Figs. 5 and 6 can be observed after 14 ns, which is much shorter than the shortest decoherent (5.7  $\mu$ s) and dephasing (1.4  $\mu$ s) times provided by the experiment [21].

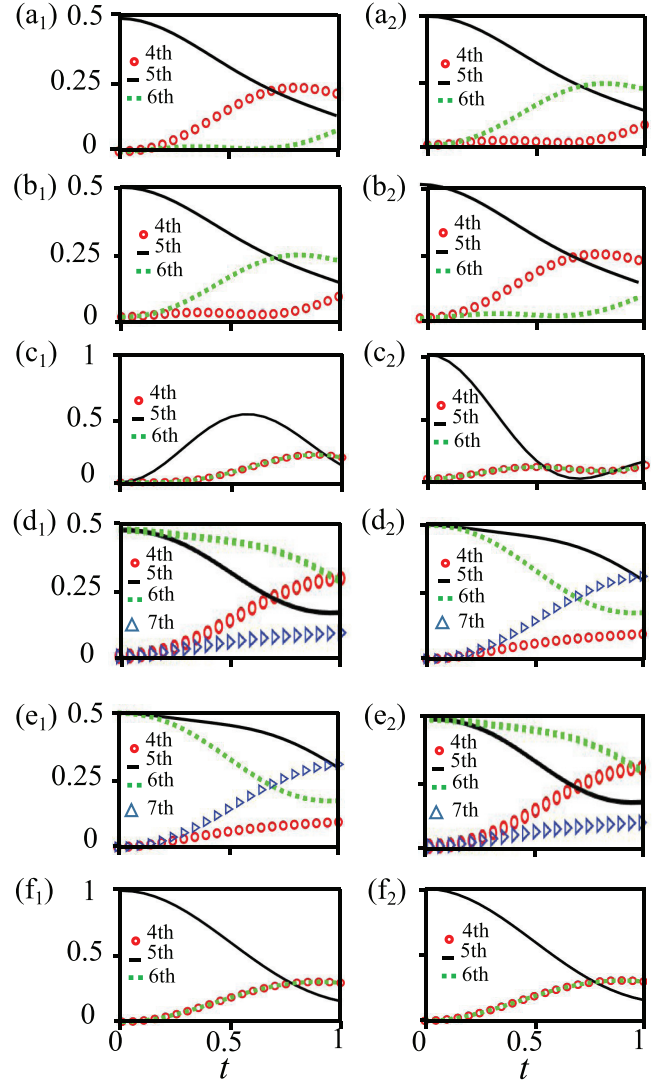


FIG. 8. Excitation numbers of the qubits at the fourth (open red circle curve), fifth (solid black line), sixth (dotted green curve), and seventh (open blue triangle curve) rungs as functions of  $t$ . (a<sub>1</sub>), (b<sub>1</sub>), (c<sub>1</sub>), (d<sub>1</sub>), (e<sub>1</sub>), and (f<sub>1</sub>) show the excitation numbers on leg A; (a<sub>2</sub>), (b<sub>2</sub>), (c<sub>2</sub>), (d<sub>2</sub>), (e<sub>2</sub>), and (f<sub>2</sub>), those on leg B. (a<sub>1</sub>)–(c<sub>2</sub>) and (d<sub>1</sub>)–(f<sub>2</sub>) with the initial states correspond with those considered in Figs. 5 [(a<sub>1</sub>), (b<sub>1</sub>), and (c<sub>1</sub>)] and 6 [(a<sub>1</sub>), (b<sub>1</sub>), and (c<sub>1</sub>)], respectively. Here  $1/t_0$  is used as the unit.

## VI. CONCLUSIONS

In summary, we have proposed an experimentally feasible method to prepare the synthetic gauge field in two-leg superconducting circuits with transmon qubits. In particular, the realized magnetic flux per plaquette is controlled independently by properly choosing the phases of the alternating-current microwave driving in each qubit, which is better than the previous realizations in the other quantum simulation systems. Moreover, we have obtained the ground-state chiral currents for the single- and two-qubit excitations and found the Meissner-vortex phase transition. In the Meissner (vortex) phase, the ground-state chiral current increases (decreases) as the magnetic flux increases. We have also explored the chiral dynamics, which depends crucially on the

initial state of the system. Finally, possible experimental observations of the chiral current and dynamics are addressed. Our results pave a new route to explore novel many-body properties [97–104], which can be induced by the interplay of the gauge field, two-leg hoppings, and interaction of photons in superconducting circuits.

## ACKNOWLEDGMENTS

This work was supported partly by the National Key R&D Program of China under Grant No. 2017YFA0304203 and the NSFC under Grants No. 11674200, No. 11947226, No. 11874156, and No. 1331KSC.

- 
- [1] Z. L. Xiang, S. Ashhab, J. Q. You, and F. Nori, *Rev. Mod. Phys.* **85**, 623 (2013).
- [2] X. Gu, A. F. Kockum, A. Miranowicz, Y. Liu, and F. Nori, *Phys. Rep.* **718**, 1 (2017).
- [3] G. Wendin, *Rep. Phys.* **80**, 106001 (2017).
- [4] A. Blais, S. M. Girvin, and W. D. Oliver, *Nat. Phys.* **16**, 247 (2020).
- [5] I. Buluta, S. Ashhab, and F. Nori, *Rep. Prog. Phys.* **74**, 104401 (2011).
- [6] F. Arute, K. Arya, R. Babbush, D. Bacon, J. C. Bardin, R. Barends, R. Biswas, S. Boixo, F. G. S. L. Brandao, D. A. Buell *et al.*, *Nature (London)* **574**, 505 (2019).
- [7] S. Schmidt and J. Koch, *Ann. Phys. (Berlin)* **525**, 395 (2013).
- [8] I. M. Georgescu, S. Ashhab, and F. Nori, *Rev. Mod. Phys.* **86**, 153 (2014).
- [9] I. Carusotto, A. A. Houck, A. J. Kollár, P. Roushan, D. I. Schuster, and J. Simon, *Nat. Phys.* **16**, 268 (2020).
- [10] Y. Salathé, M. Mondal, M. Oppliger, J. Heinsoo, P. Kurpiers, A. Potočnik, A. Mezzacapo, U. Las Heras, L. Lamata, E. Solano, S. Filipp, and A. Wallraff, *Phys. Rev. X* **5**, 021027 (2015).
- [11] A. Kandala, A. Mezzacapo, K. Temme, M. Takita, M. Brink, J. M. Chow, and J. M. Gambetta, *Nature (London)* **549**, 242 (2017).
- [12] P. Roushan, C. Neill, J. Tangpanitanon, V. M. Bastidas, A. Megrant, R. Barends, Y. Chen, Z. Chen, B. Chiaro, A. Dunsworth *et al.*, *Science* **358**, 1175 (2017).
- [13] K. Xu, J.-J. Chen, Y. Zeng, Y.-R. Zhang, C. Song, W. Liu, Q. Guo, P. Zhang, D. Xu, H. Deng, K. Huang, H. Wang, X. Zhu, D. Zheng, and H. Fan, *Phys. Rev. Lett.* **120**, 050507 (2018).
- [14] P. J. J. O'Malley, R. Babbush, I. D. Kivlichan, J. Romero, J. R. McClean, R. Barends, J. Kelly, P. Roushan, A. Tranter, N. Ding *et al.*, *Phys. Rev. X* **6**, 031007 (2016).
- [15] Y. P. Zhong, D. Xu, P. Wang, C. Song, Q. J. Guo, W. X. Liu, K. Xu, B. X. Xia, C.-Y. Lu, S. Han *et al.*, *Phys. Rev. Lett.* **117**, 110501 (2016).
- [16] C. Song, D. Xu, P. Zhang, J. Wang, Q. Guo, W. Liu, K. Xu, H. Deng, K. Huang, D. Zheng *et al.*, *Phys. Rev. Lett.* **121**, 030502 (2018).
- [17] W. Cai, J. Han, F. Mei, Y. Xu, Y. Ma, X. Li, H. Wang, Y. P. Song, Z. Y. Xue, Z. Q. Yin *et al.*, *Phys. Rev. Lett.* **123**, 080501 (2019).
- [18] Z. Yan, Y. R. Zhang, M. Gong, Y. Wu, Y. Zheng, S. Li, C. Wang, F. Liang, J. Lin, Y. Xu *et al.*, *Science* **364**, 753 (2019).
- [19] R. Ma, B. Saxberg, C. Owens, N. Leung, Y. Lu, and J. Simon, *Nature (London)* **566**, 51 (2019).
- [20] M. Fitzpatrick, N. M. Sundaresan, A. C. Y. Li, J. Koch, and A. A. Houck, *Phys. Rev. X* **7**, 011016 (2017).
- [21] Y. Ye, Z. Y. Ge, Y. Wu, S. Wang, M. Gong, Y. R. Zhang, Q. Zhu, R. Yang, S. Li, F. Liang *et al.*, *Phys. Rev. Lett.* **123**, 050502 (2019).
- [22] D. N. Sheng, O. I. Motrunich, and M. P. A. Fisher, *Phys. Rev. B* **79**, 205112 (2009).
- [23] H. H. Lai and O. I. Motrunich, *Phys. Rev. B* **81**, 045105 (2010).
- [24] X. Li, E. Zhao, and W. V. Liu, *Nat. Commun.* **4**, 1523 (2013).
- [25] W. M. Huang, K. Irwin, and S. W. Tsai, *Phys. Rev. A* **87**, 031603(R) (2013).
- [26] S. Uchino and T. Giamarchi, *Phys. Rev. A* **91**, 013604 (2015).
- [27] J. P. Lv and Z. D. Wang, *Phys. Rev. B* **93**, 174507 (2016).
- [28] S. Greschner and F. Heidrich-Meisner, *Phys. Rev. A* **97**, 033619 (2018).
- [29] R. Nehra, D. S. Bhakuni, S. Gangadharaiyah, and A. Sharma, *Phys. Rev. B* **98**, 045120 (2018).
- [30] Z. Zhou, F. Chen, Y. Zhong, H. G. Luo, and J. Zhao, *Phys. Rev. B* **99**, 205143 (2019).
- [31] R. A. Santos and B. Béri, *Phys. Rev. B* **100**, 235122 (2019).
- [32] G. L. Nave, K. Limtragoon, and P. W. Phillips, *Rev. Mod. Phys.* **91**, 021003 (2019).
- [33] D. Bailin and A. Love, *Cosmology in Gauge Field Theory and String Theory* (CRC Press, Boca Raton, FL, 2004).
- [34] J. Dalibard, F. Gerbier, G. Juzeliūnas, and P. Öhberg, *Rev. Mod. Phys.* **83**, 1523 (2011).
- [35] N. Goldman, G. Juzeliūnas, Pohberg, and I. B. Spielman, *Rep. Prog. Phys.* **77**, 126401 (2014).
- [36] D.-W. Zhang, Y.-Q. Zhu, Y. X. Zhao, H. Yan, and S.-L. Zhu, *Adv. Phys.* **67**, 253 (2018).
- [37] E. Witten, *Rev. Mod. Phys.* **88**, 035001 (2016).
- [38] B. K. Stuhl, H. I. Lu, L. M. Ayccock, D. Genkina, and I. B. Spielman, *Science* **349**, 1514 (2015).
- [39] H. M. Price, O. Zilberberg, T. Ozawa, I. Carusotto, and N. Goldman, *Phys. Rev. Lett.* **115**, 195303 (2015).
- [40] T. Ozawa, H. M. Price, N. Goldman, O. Zilberberg, and I. Carusotto, *Phys. Rev. A* **93**, 043827 (2016).
- [41] B. J. Diaz, T. Graß, N. Barberán, and M. Lewenstein, *New. J. Phys.* **14**, 055003 (2012).
- [42] L. Hormozi, G. Möller, and S. H. Simon, *Phys. Rev. Lett.* **108**, 256809 (2012).
- [43] F. Grusdt, F. Letscher, M. Hafezi, and M. Fleischhauer, *Phys. Rev. Lett.* **113**, 155301 (2014).
- [44] S. Powell, R. Barnett, R. Sensarma, and S. Das Sarma, *Phys. Rev. Lett.* **104**, 255303 (2010).
- [45] R. O. Umucalilar and I. Carusotto, *Phys. Rev. A* **84**, 043804 (2011).
- [46] A. Celi, P. Massignan, J. Ruseckas, N. Goldman, I. B. Spielman, G. Juzeliūnas, and M. Lewenstein, *Phys. Rev. Lett.* **112**, 043001 (2014).
- [47] A. Dhar, T. Mishra, M. Maji, R. V. Pai, S. Mukerjee, and A. Paramekanti, *Phys. Rev. B* **87**, 174501 (2013).
- [48] M. Piraud, F. Heidrich-Meisner, I. P. McCulloch, S. Greschner, T. Vekua, and U. Schollwöck, *Phys. Rev. B* **91**, 140406(R) (2015).

- [49] A. Petrescu and K. L. Hur, *Phys. Rev. B* **91**, 054520 (2015).
- [50] Y.-P. Wang, W. Wang, Z.-Y. Xue, W.-L. Yang, Y. Hu, and Y. Wu, *Sci. Rep.* **5**, 8352 (2015).
- [51] Y.-P. Wang, W.-L. Yang, Y. Hu, Z.-Y. Xue, and Y. Wu, *npj Quantum Inf.* **2**, 16015 (2016).
- [52] P. Roushan, C. Neill, A. Megrant, Y. Chen, R. Babbush, R. Barends, B. Campbell, Z. Chen, B. Chiaro, A. Dunsworth *et al.*, *Nat. Phys.* **13**, 146 (2017).
- [53] D. W. Wang, C. Song, W. Feng, H. Cai, D. Xu, H. Deng, H. Li, D. Zheng, X. Zhu, H. Wang *et al.*, *Nat. Phys.* **15**, 382 (2019).
- [54] M. Aidelsburger, M. Atala, S. Nascimbène, S. Trotzky, Y. A. Chen, and I. Bloch, *Phys. Rev. Lett.* **107**, 255301 (2011).
- [55] M. Aidelsburger, M. Atala, M. Lohse, J. T. Barreiro, B. Paredes, and I. Bloch, *Phys. Rev. Lett.* **111**, 185301 (2013).
- [56] H. Miyake, G. A. Siviloglou, C. J. Kennedy, W. C. Burton, and W. Ketterle, *Phys. Rev. Lett.* **111**, 185302 (2013).
- [57] M. Atala, M. Aidelsburger, M. Lohse, J. T. Barreiro, B. Paredes, and I. Bloch, *Nat. Phys.* **10**, 588 (2014).
- [58] M. Mancini, G. Pagano, G. Cappellini, L. Livi, M. Rider, J. Catani, C. Sias, P. Zoller, M. Inguscio, M. Dalmonte, and L. Fallan, *Science* **349**, 1510 (2015).
- [59] M. Hafezi, S. Mittal, J. Fan, A. Migdall, and J. M. Taylor, *Nat. Photon.* **7**, 1001 (2013).
- [60] K. Fang, J. Luo, A. Metelmann, M. H. Matheny, F. Marquardt, A. A. Clerk, and O. Painter, *Nat. Phys.* **13**, 465 (2017).
- [61] L. Yuan, Q. Lin, A. Zhang, M. Xiao, X. Chen, and S. Fan, *Phys. Rev. Lett.* **122**, 083903 (2019).
- [62] Y. Chen, Y.-L. Zhang, Z. Shen, C.-L. Zou, G.-C. Guo, and C.-H. Dong, *arXiv:1908.04456*.
- [63] X. Wen, C. Qiu, Y. Qi, L. Ye, M. Ke, F. Zhang, and Z. Liu, *Nat. Phys.* **15**, 352 (2019).
- [64] A. Bermudez, T. Schaetz, and D. Porras, *Phys. Rev. Lett.* **107**, 150501 (2011).
- [65] M. Levin and A. Stern, *Phys. Rev. Lett.* **103**, 196803 (2009).
- [66] J. Klinovaja, A. Yacoby, and D. Loss, *Phys. Rev. B* **90**, 155447 (2014).
- [67] R. A. Santos, C.-W. Huang, Y. Gefen, and D. B. Gutman, *Phys. Rev. B* **91**, 205141 (2015).
- [68] L. V. Levitin, R. G. Bennett, A. Casey, B. Cowan, J. Saunders, D. Drung, T. Schurig, and J. M. Parpia, *Science* **340**, 841 (2013).
- [69] S. Autti, V. V. Dmitriev, J. T. Mäkinen, A. A. Soldatov, G. E. Volovik, A. N. Yudin, V. V. Zavjalov, and V. B. Eltsov, *Phys. Rev. Lett.* **117**, 255301 (2016).
- [70] W. Jia, Z.-H. Huang, X. Wei, Q. Zhao, and X.-J. Liu, *Phys. Rev. B* **99**, 094520 (2019).
- [71] B. Fauqué, Y. Sidis, V. Hinkov, S. Pailhès, C. T. Lin, X. Chaud, and P. Bourges, *Phys. Rev. Lett.* **96**, 197001 (2006).
- [72] E. Morenzoni, B. M. Wojek, A. Suter, T. Prokscha, G. Logvenov, and I. Božović, *Nat. Commun.* **2**, 272 (2011).
- [73] X. Li, Y. Ma, J. Han, T. Chen, Y. Xu, W. Cai, H. Wang, Y. P. Song, Z.-Y. Xue, Z.-Q. Yin, and L. Sun, *Phys. Rev. Appl.* **10**, 054009 (2018).
- [74] D. Hügél and B. Paredes, *Phys. Rev. A* **89**, 023619 (2014).
- [75] L. K. Lim, A. Hemmerich, and C. M. Smith, *Phys. Rev. A* **81**, 023404 (2010).
- [76] G. Möller and N. R. Cooper, *Phys. Rev. A* **82**, 063625 (2010).
- [77] M. Aidelsburger, M. Atala, S. Nascimbène, S. Trotzky, Y. A. Chen, and I. Bloch, *Appl. Phys. B* **113**, 1 (2013).
- [78] R. Sachdeva, F. Metz, M. Singh, T. Mishra, and T. Busch, *Phys. Rev. A* **98**, 063612 (2018).
- [79] E. Orignac and T. Giamarchi, *Phys. Rev. B* **64**, 144515 (2001).
- [80] E. Orignac, R. Citro, M. D. Dio, and S. D. Palo, *Phys. Rev. B* **96**, 014518 (2017).
- [81] R. Barends, J. Kelly, A. Megrant, A. Veitia, D. Sank, E. Jeffrey, T. C. White, J. Mutus, A. G. Fowler, B. Campbell *et al.*, *Nature (London)* **508**, 500 (2014).
- [82] B. R. Johnson, M. P. da Silva, C. A. Ryan, S. Kimmel, J. M. Chow, and T. A. Ohki, *New J. Phys.* **17**, 113019 (2015).
- [83] J. Z. Blumoff, K. Chou, C. Shen, M. Reagor, C. Axline, R. T. Brierley, M. P. Silveri, C. Wang, B. Vlastakis, S. E. Nigg *et al.*, *Phys. Rev. X* **6**, 031041 (2016).
- [84] M. A. Rol, C. C. Bultink, T. E. O'Brien, S. R. de Jong, L. S. Theis, X. Fu, F. Luthi, R. F. L. Vermeulen, J. C. de Sterke, A. Bruno *et al.*, *Phys. Rev. Appl.* **7**, 041001 (2017).
- [85] D. C. McKay, C. J. Wood, S. Sheldon, J. M. Chow, and J. M. Gambetta, *Phys. Rev. A* **96**, 022330 (2017).
- [86] M. Steffen, M. Ansmann, R. McDermott, N. Katz, R. C. Bialczak, E. Lucero, M. Neeley, E. M. Weig, A. N. Cleland, and J. M. Martinis, *Phys. Rev. Lett.* **97**, 050502 (2006).
- [87] C. Song, K. Xu, W. Liu, C. P. Yang, S. B. Zheng, H. Deng, Q. Xie, K. Huang, Q. Guo, L. Zhang, P. Zhang, D. Xu, D. Zheng, X. Zhu, H. Wang, Y. A. Chen, C. Y. Lu, S. Han, and J. W. Pan, *Phys. Rev. Lett.* **119**, 180511 (2017).
- [88] T. Xin, D. Lu, J. Klassen, N. Yu, Z. Ji, J. Chen, X. Ma, G. Long, B. Zeng, and R. Laflamme, *Phys. Rev. Lett.* **118**, 020401 (2017).
- [89] C. Riofrío, D. Gross, S. T. Flammia, T. Monz, D. Nigg, R. Blatt, and J. Eisert, *Nat. Commun.* **8**, 1 (2017).
- [90] D. Ahn, Y. S. Teo, H. Jeong, F. Bouchard, F. Hufnagel, E. Karimi, D. Koutný, J. Řeháček, Z. Hradil, G. Leuchs, and L. L. Sánchez-Soto, *Phys. Rev. Lett.* **122**, 100404 (2019).
- [91] G. Torlai, B. Timar, E. P. L. van Nieuwenburg, H. Levine, A. Omran, A. Keesling, H. Bernien, M. Greiner, V. Vuletić, M. D. Lukin, R. G. Melko, and M. Endres, *Phys. Rev. Lett.* **123**, 230504 (2019).
- [92] A. M. Palmieri, E. Kovlakov, F. Bianchi, D. Yudin, S. Straupe, J. D. Biamonte, and S. Kulik, *npj Quantum Inf.* **6**, 20 (2020).
- [93] T. Xin, S. Lu, N. Cao, G. Anikeeva, D. Lu, J. Li, G. Long, and B. Zeng, *npj Quantum Info.* **5**, 109 (2019).
- [94] B. P. Lanyon, C. Maier, M. Holzzapfel, T. Baumgratz, C. Hempel, P. Jurcevic, I. Dhand, A. S. Buyskikh, A. J. Daley, M. Cramer *et al.*, *Nat. Phys.* **13**, 1158 (2017).
- [95] T. Xin, X. Nie, X. Kong, J. Wen, D. Lu, and J. Li, *Phys. Rev. Appl.* **13**, 024013 (2020).
- [96] Y. Liu, D. Wang, S. Xue, A. Huang, X. Fu, X. Qiang, P. Xu, H.-L. Huang, M. Deng, C. Guo, X. Yang, and J. Wu, *Phys. Rev. A* **101**, 052316 (2020).
- [97] S. S. Natu, *Phys. Rev. A* **92**, 053623 (2015).
- [98] A. Keles and M. Ö. Oktel, *Phys. Rev. A* **91**, 013629 (2015).
- [99] S. Greschner, M. Piraud, F. Heidrich-Meisner, I. P. McCulloch, U. Schollwöck, and T. Vekua, *Phys. Rev. A* **94**, 063628 (2016).
- [100] S. Greschner and T. Vekua, *Phys. Rev. Lett.* **119**, 073401 (2017).

- [101] R. Sachdeva, M. Singh, and T. Busch, *Phys. Rev. A* **95**, 063601 (2017).
- [102] Y. Zheng, S. Feng, and S. J. Yang, *Phys. Rev. A* **96**, 063613 (2017).
- [103] R. Citro, S. De Palo, M. Di Dio, and E. Orignac, *Phys. Rev. B* **97**, 174523 (2018).
- [104] M. C. Strinati, S. Sahoo, K. Shtengel, and E. Sela, *Phys. Rev. B* **99**, 245101 (2019).